Chemical Science

ROYAL SOCIETY OF CHEMISTRY

EDGE ARTICLE

View Article Online
View Journal | View Issue

Cite this: *Chem. Sci.*, 2025, **16**, 16339

All publication charges for this article have been paid for by the Royal Society of Chemistry

A non-ionic fluorinated p-dopant enables the construction of efficient and stable perovskite solar cells

Zhongquan Wan, * Wang Yu, Jinyu Yang, Yunpeng Zhang, Yuanxi Wang, Runmin Wei, Muhammad Azam, Junsheng Luo * and Chunyang Jia *

Received 17th June 2025
Accepted 6th August 2025

DOI: 10.1039/d5sc04440e

rsc.li/chemical-science

The Li-TFSI/*t*-BP system is essential for doping the hole-transporting layer (HTL) to construct efficient perovskite solar cells (PSCs). However, the hygroscopicity and Li^+ migration of Li-TFSI, as well as the corrosiveness and volatility of *t*-BP, can have negative impacts on the efficiency and stability of PSCs. Herein, a novel non-ionic fluorinated p-dopant 1-[bis(trifluoromethanesulfonyl)methyl]-2,3,4,5,6-pentafluorobenzene (PFB-TFSI) is developed to replace the Li-TFSI/*t*-BP system. The non-ionic structure of PFB-TFSI allows it to dissolve in chlorobenzene without *t*-BP. Moreover, due to the lower HOMO level of PFB-TFSI, it can directly oxidize PTAA to generate $[PTAA]^+$ radical cations without post-treatment, achieving effective doping of PTAA. The moisture resistance of the HTL is also improved due to the presence of multiple fluorine atoms in PFB-TFSI. Ultimately, compared to 21.98% efficiency of the PSC based on PTAA:Li-TFSI/*t*-BP, the PSC based on PTAA:PFB-TFSI achieved higher efficiency (24.22%). Furthermore, the long-term stability of the PSC based on PTAA:PFB-TFSI is greatly improved, retaining 88% of its initial efficiency after aging for 300 hours at 85 °C and 50–70% relative humidity, whereas the PSC based on PTAA:Li-TFSI/*t*-BP only retains 63%.

1. Introduction

Organic–inorganic hybrid perovskite solar cells have experienced rapid development due to their advantages such as high photovoltaic conversion efficiency, simple fabrication process, tunable direct bandgap, high charge carrier mobility, long diffusion length, and relatively low cost. The photovoltaic conversion efficiency (PCE) of PSCs has increased from 3.8% to 26.95%.[1–6] In PSCs, the hole-transporting layer (HTL) effectively blocks electrons while collecting holes, achieving efficient electron–hole separation. Simultaneously, it impedes moisture diffusion into PSCs, reducing degradation caused by moisture in air.[7–10]

Presently, PTAA and Spiro-OMeTAD are used as classic HTL materials in PSCs.[11] However, their intrinsic hole mobility and conductivity are low, necessitating the addition of hole doping agents to enhance p-type doping and improve hole-transporting performance to increase PSCs' efficiency.[12] Currently the most widely used doping system is the Li-TFSI/*t*-BP system. *t*-BP facilitates the dissolution of Li-TFSI in non-polar solutions like chlorobenzene. Li-TFSI does not directly dope but promotes oxidative doping of the HTM under sunlight.[13–15] While achieving high efficiency, the Li-TFSI/*t*-BP system also has negative issues: Li^+ has a small ion radius, easily diffuses into the other layer, and has strong hygroscopicity which can absorb moisture from air and damage the perovskite layer.[16,17] Meanwhile, the polar solvent *t*-BP with a low boiling point will evaporate in the HTL, leaving voids and damaging the perovskite layer.[18–20] Besides, indirect doping is highly dependent on environmental conditions, is time-consuming, and lacks repeatability.[21] These issues degrade the performance and stability of PSCs and hinder their commercialization.[22] Current studies are focused on solving the problems caused by hygroscopic Li^+.[23–25] For instance, strategies include adding small amounts of PbI_2 to the Li-TFSI/*t*-BP system to inhibit Li-TFSI aggregation and *t*-BP evaporation,[26] incorporating reduced graphene oxide to mitigate Li^+ ion hygroscopicity[27] and introducing MoS_2 to absorb Li^+ ions and suppress their migration.[28] However, extra additives bring new challenges and increase costs and complexity. Therefore, developing stable and efficient p-dopants to replace the Li-TFSI/*t*-BP system remains a better choice.[29]

In this study, a novel fluorinated molecule 1-[bis(trifluoromethanesulfonyl)methyl]-2,3,4,5,6-pentafluorobenzene (PFB-TFSI) is developed as a p-dopant (Fig. 1a). Serving as a non-ionic p-dopant, PFB-TFSI addresses issues related to Li^+ ion migration and hygroscopicity. Unlike Li-TFSI, it can dissolve directly in chlorobenzene without *t*-BP, and the positive charges on the molecular surface are more

National Key Laboratory of Electronic Films and Integrated Devices, School of Integrated Circuit Science and Engineering, University of Electronic Science and Technology of China, 611731 Chengdu, P. R. China. E-mail: zqwan@uestc.edu.cn; luojs@uestc.edu.cn; cyjia@uestc.edu.cn

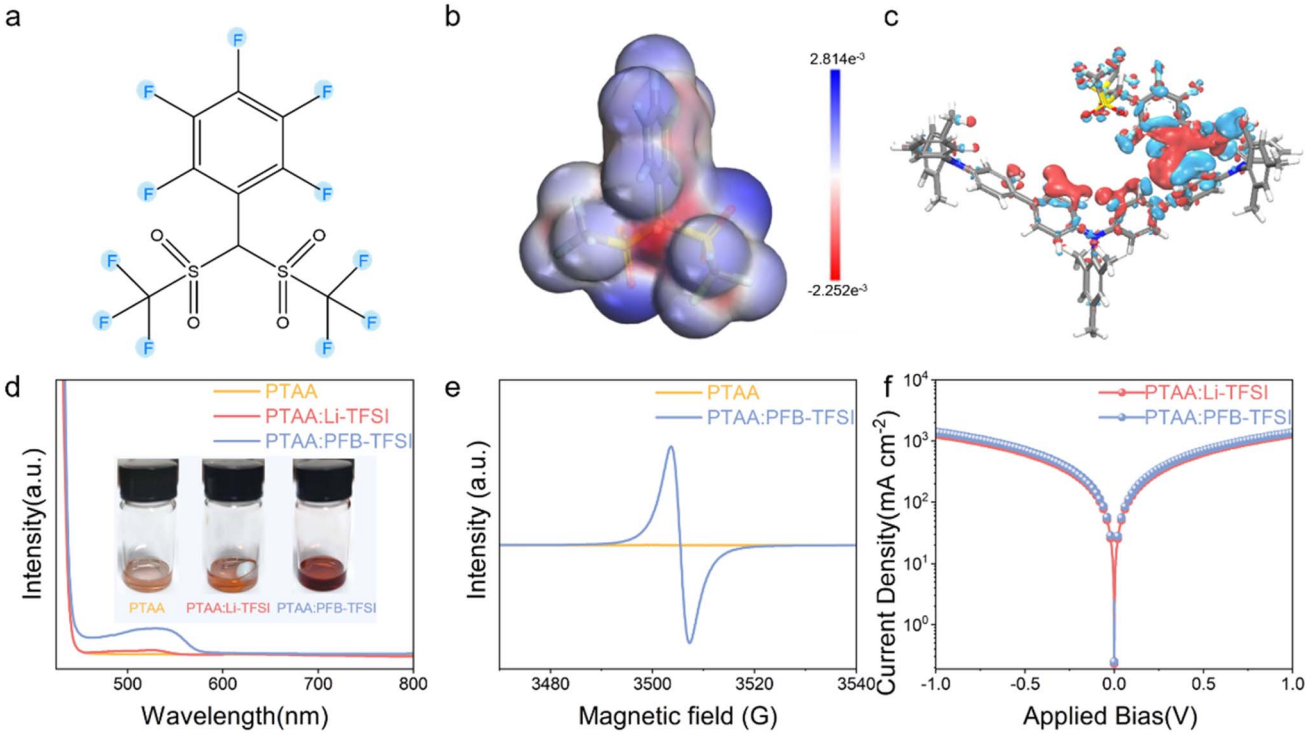

Fig. 1 (a) Chemical structure of PFB-TFSI. (b) ESP surface of PFB-TFSI. (c) Differential charge diagram of PTAA:PFB-TFSI. (d) UV-vis absorption spectra of PTAA, PTAA:Li-TFSI/*t*-BP and PTAA:PFB-TFSI solutions. The illustration shows the color of PTAA solution treated with different dopants. (e) ESR spectra of PTAA:Li-TFSI/*t*-BP and PTAA:PFB-TFSI solutions. (f) Conductivity tests of PTAA:Li-TFSI/*t*-BP and PTAA:PFB-TFSI films.

concentrated (Fig. 1b), giving the molecule Lewis acid properties that facilitate the spontaneous transfer of charges to form hole states, achieving effective p-type doping. Furthermore, PFB-TFSI possesses a suitable HOMO energy level to accommodate electron transfer within PTAA, enabling direct oxidation to yield $[PTAA]^+$ radical cations under anaerobic conditions. Ultimately, the PSC utilizing PTAA:PFB-TFSI achieved a PCE of 24.22%, while exhibiting good stability under unencapsulated atmospheric conditions.

2. Results and discussion

Initially, PFB-TFSI and Li-TFSI/*t*-BP were dissolved in PTAA solution separately. The color of the PTAA solution immediately turned brown after adding PFB-TFSI, while the solution with Li-TFSI/*t*-BP remained light yellow (Fig. 1d). The change in color suggests that charge transfer may have occurred in the solution, which preliminarily indicates that PFB-TFSI directly achieves p-type doping of PTAA, generating $[PTAA]^+$ radical cations. To confirm this conclusion, UV-visible absorption and electron spin resonance (ESR) were conducted. The PTAA:PFB-TFSI solution exhibits a new strong absorption peak near 540 nm compared to undoped PTAA solution (Fig. 1d), which is attributed to the direct oxidation process of PFB-TFSI, while the PTAA:Li-TFSI/*t*-BP solution only shows a very weak absorption peak near 540 nm. Moreover, PTAA:PFB-TFSI solution shows a strong $[PTAA]^+$ radical signal at 3500–3520 G (Fig. 1e), confirming the presence of $[PTAA]^+$ radical cations.[30,31] From the above analysis, it can be concluded that PTAA can be doped with PFB-TFSI in an anaerobic environment without *t*-BP and acetonitrile, generating $[PTAA]^+$ radical cations in the solution.

To verify the intermolecular charge transfer, the differential charge of PTAA:PFB-TFSI was calculated, and the PTAA structure has been replaced by trimers for ease of calculation, where blue and red represent charge accumulation and depletion respectively (Fig. 1c). When PFB-TFSI interacts with PTAA, the electrons are mainly concentrated on PFB-TFSI, while the holes are primarily concentrated at the interface between PTAA and PFB-TFSI, which indicates the presence of charge transfer between PFB-TFSI and PTAA. Furthermore, the conductivity of the HTL was tested to evaluate the doping effect of different dopants on PTAA (Fig. 1f). Compared to the PTAA:Li-TFSI/*t*-BP film (8.87×10^{-6} S cm^{-1}), the PTAA:PFB-TFSI film exhibits higher conductivity (9.95×10^{-6} S cm^{-1}), which further confirms that PFB-TFSI can directly oxidize PTAA to generate $[PTAA]^+$ radical cations, achieving more effective doping of PTAA.

To investigate the doping mechanism of PFB-TFSI on PTAA, the highest occupied molecular orbital (HOMO) energy levels of PFB-TFSI and PTAA were measured using cyclic voltammetry (CV). As shown in Fig. S1, based on the first oxidation potentials (E_{ox}), the HOMO energy levels can be calculated using formula (1):

$$E_{HOMO} = -(E_{ox} + 4.70) \quad (1)$$

where the values of E_{ox} for PFB-TFSI and PTAA were 0.62 and 0.55 V and the corresponding HOMO energy levels were

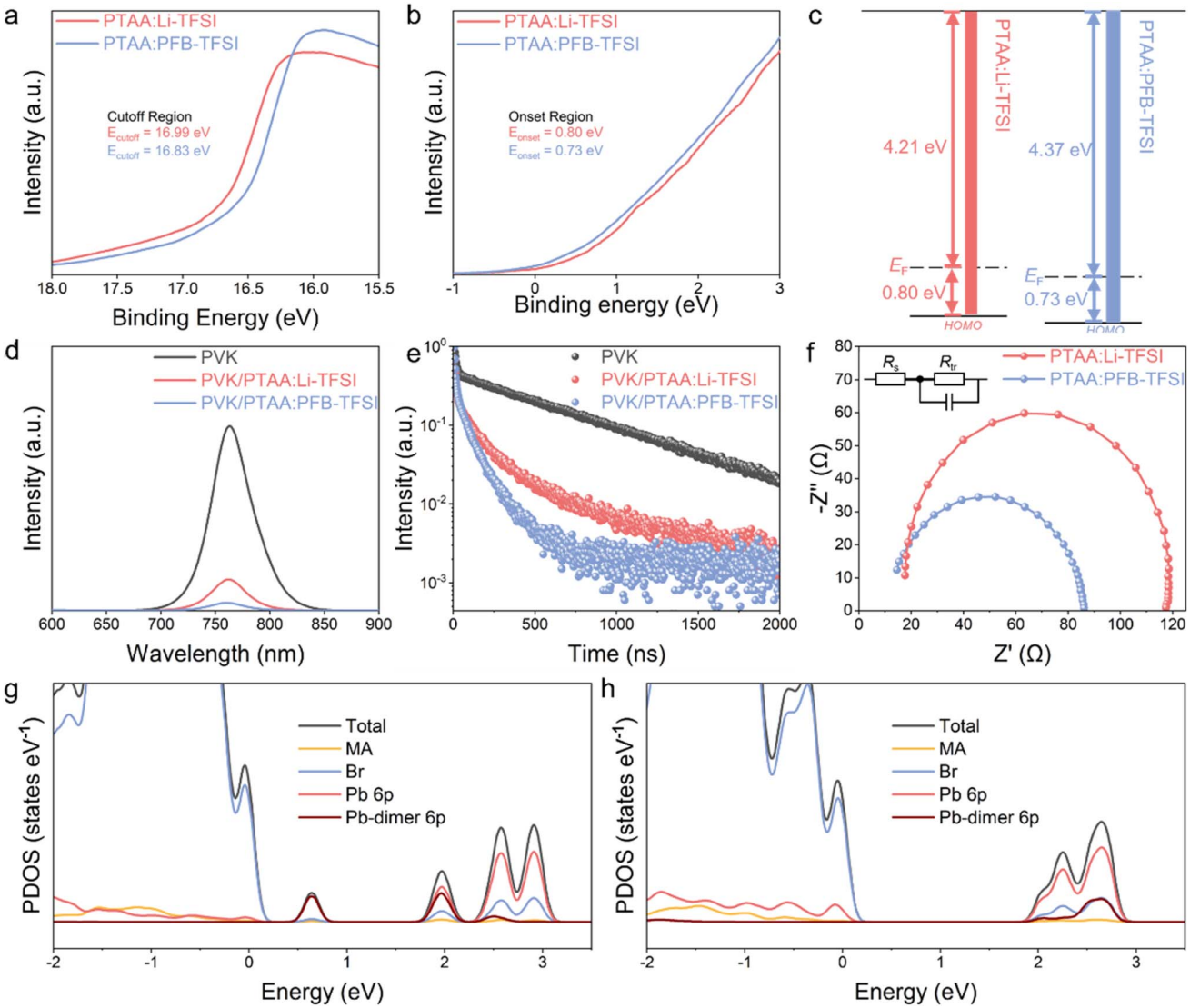

Fig. 2 (a) Cutoff regions and (b) onset regions of the UPS spectra for PTAA:Li-TFSI/*t*-BP and PTAA:PFB-TFSI films. (c) Energy level diagrams of PTAA:Li-TFSI/*t*-BP and PTAA:PFB-TFSI films. (d) Steady-state PL and (e) TRPL spectra of glass/perovskite, glass/perovskite/PTAA:Li-TFSI/*t*-BP and glass/perovskite/PTAA:PFB-TFSI samples. (f) Nyquist plots of PSCs based on PTAA:Li-TFSI/*t*-BP and PTAA:PFB-TFSI. PDOS diagrams of Pb–Pb dimer defects (g) before and (h) after PFB-TFSI absorption.

calculated to be −5.32 and −5.25 eV, respectively. The lower HOMO energy level of PFB-TFSI facilitates direct electron transfer from PTAA, indicating that PFB-TFSI can directly oxidize PTAA to generate $[PTAA]^+$ under anaerobic conditions, thereby avoiding the subsequent slow oxidation step. In addition, as shown in Fig. S1, compared with the E_{ox} of PTAA and PFB-TFSI solutions, the E_{ox} of PTAA:PFB-TFSI the solution mixture changed (0.58 V), indicating charge transfer between PTAA and PFB-TFSI. The above experiments and theoretical calculations demonstrate that PFB-TFSI can be used for direct oxidation of PTAA.[32,33]

Introducing PFB-TFSI into the HTL can regulate the HOMO energy level, promote the energy level alignment between the HTL and perovskite, and thus improve charge carrier transport efficiency. In order to elucidate the regulatory effect of the two different p-dopants on the HOMO energy level of PTAA, the PTAA films with different p-dopants were further characterized using ultraviolet photoelectron spectroscopy (UPS). Fig. 2a and b show the UPS spectra of PTAA films doped with different p-dopants, including the cutoff (E_{cutoff}) and onset (E_{onset}) energy regions. The position of the HOMO energy level can be calculated using formula (2):

$$E_{HOMO} = h\nu - (E_{cutoff} - E_{onset}) \quad (2)$$

where $h\nu$ is the He(I) photon energy (21.22 eV). Ultimately, the HOMO energy level of the PTAA:PFB-TFSI film was calculated to be −5.10 eV, indicating a certain degree of reduction compared to PTAA:Li-TFSI/*t*-BP (−5.01 eV).[34,35] As shown in the energy level diagram (Fig. 2c), the lower HOMO energy level optimizes the energy level alignment between the perovskite layer and HTL, reduces the Schottky barrier, and thus reduces energy loss

during hole extraction, ultimately leading to higher open-circuit voltage (V_{oc}).

To further investigate charge transfer at the interface, steady-state photoluminescence (PL) and transient photoluminescence (TRPL) were employed to study the hole extraction capability between the perovskite layer and HTL. From the PL spectra shown in Fig. 2d, it can be seen that the emission peak intensity at 764 nm shows the order of glass/perovskite > glass/perovskite/PTAA:Li-TFSI/*t*-BP > glass/perovskite/PTAA:PFB-TFSI samples, indicating that PFB-TFSI doping enhances hole extraction from the perovskite. Moreover, compared to the glass/perovskite/PTAA:Li-TFSI/*t*-BP sample, the PL peak of the glass/perovskite/PTAA:PFB-TFSI sample exhibited a blue shift (PL peak shifted from 760 nm to 764 nm), which is due to PFB-TFSI not only having a doping effect on PTAA but also passivating defect states on the perovskite surface.[36]

Fig. 2e shows the TRPL spectra of the samples with the same structure in PL spectra. The average decay time τ_{ave} was fitted with a three exponential decay model. The glass/perovskite sample exhibits the longest τ_{ave} of 597.2 ns, while the τ_{ave} of the glass/perovskite/PTAA:Li-TFSI/*t*-BP sample is 92.08 ns. The τ_{ave} of glass/perovskite/PTAA:PFB-TFSI is further reduced (41.91 ns), indicating that the HTL doped with PFB-TFSI has enhanced hole extraction capability. This suggests that PTAA doped with PFB-TFSI can extract and collect holes faster than PTAA doped Li-TFSI/*t*-BP.[37]

Electrochemical impedance spectroscopy (EIS) was utilized to investigate charge transfer processes at the perovskite/HTL interface.[38] EIS measurements were performed on PSCs based on PTAA:Li-TFSI/*t*-BP and PTAA:PFB-TFSI, and the results were fitted using ZView software (Fig. 2f). In the impedance equivalent circuit, R_s represents the series resistance, reflecting the impedance during charge transport within the device, while R_{tr} represents the charge transport resistance at the perovskite/HTL interface. Compared to the PSC based on PTAA:Li-TFSI/*t*-BP ($R_s = 19\ \Omega$; $R_{tr} = 99\ \Omega$), the PSC based on PTAA:PFB-TFSI has lower R_s (12 Ω) and R_{tr} (75 Ω), attributed to the lower HOMO energy level of the PTAA:PFB-TFSI film, which optimizes the energy level alignment and improves charge transport. The low R_s and R_{tr} are beneficial for PSCs to achieve a higher fill factor (FF) and PCE.

The numerous defects on the surface of perovskites can serve as recombination centers for charge carriers, affecting hole extraction and transport.[39] Reducing the defects is beneficial for enhancing the hole extraction capability at the perovskite/HTL interface.[40] To investigate the passivation effect of PFB-TFSI on perovskite/HTL interface defects, a Pb–Pb dimer was placed at the perovskite (001) interface to simulate deep-level defect states on the perovskite surface. Fig. 2g shows the projected density of states (PDOS) diagram of the perovskite (001) crystal plane with the Pb–Pb dimer. The addition of the Pb–Pb dimer introduces a deep-level defect in the perovskite bandgap, capturing holes at the perovskite/HTL interface, thus degrading carrier transport performance.[41] The differential charge diagram in Fig. S2 also shows similar results, with excess charges on the perovskite surface mainly concentrated around the Pb–Pb dimer, acting as non-radiative recombination centers for photogenerated carriers. However, when PFB-TFSI interacts with the Pb–Pb dimer, the fluorine and oxygen elements in PFB-TFSI interact with the Pb–Pb dimer, causing it to shift from the equilibrium position towards the interior of the perovskite (Fig. S3 and S4), thereby suppressing surface charge accumulation. As shown in Fig. S5, excess charges on the perovskite surface are transferred to PFB-TFSI. The interaction between PFB-TFSI and the Pb–Pb dimer converts the deep-level defect into a shallow-level defect, causing the gap defect state composed of the Pb–Pb dimer to disappear (Fig. 2h), effectively reducing non-radiative recombination, enhancing hole-transporting capability and consequently improving photovoltaic performance of PSCs.

To investigate the impact of PFB-TFSI on the photovoltaic performances of PSCs, PSCs with varying concentrations of PFB-TFSI doping were prepared with an ITO/SnO_2/perovskite/PTAA:PFB-TFSI/Au device structure. Fig. 3a shows the cross-section SEM of the entire device. The *J*–*V* curves under standard simulated sunlight conditions were obtained (Fig. 3b), with detailed corresponding data in Table S1. The PCE of PSCs shows an initial increase and then a decrease with the rise in the PFB-TFSI doping concentration. The highest PCE of 24.22% ($V_{oc} = 1.16$ V, $J_{sc} = 25.97$ mA cm^{-2}, and FF = 0.804) was achieved at a doping concentration of 1 mol%, which is superior to the PCE of the PSC based on PTAA:Li-TFSI/*t*-BP (PCE = 21.98%, $V_{oc} = 1.11$ V, $J_{sc} = 25.35$ mA cm^{-2}, and FF = 0.781) (Fig. 3c). The higher PCE of the PSC based on PTAA:PFB-TFSI is primarily attributed to its better energy level alignment and the passivation of perovskite surface defects by PFB-TFSI.[42,43]

Moreover, measurements of the steady-state PCE at the maximum power point under continuous solar illumination further verified the reliability of the photovoltaic performance (Fig. 3d). Compared to the PSC based on PTAA:Li-TFSI/*t*-BP, the PSC based on PTAA:PFB-TFSI demonstrated faster photoelectric response and superior steady-state output capability. The incident photon-to-electron conversion efficiency (IPCE) for PSCs based on PTAA:Li-TFSI/*t*-BP and PTAA:PFB-TFSI was examined to confirm the accuracy of J_{sc} values of PSCs. As shown in Fig. 3e, the calculated integrated J_{sc} value of the PSC based on PTAA:PFB-TFSI was 25.76 mA cm^{-2}, which was in good agreement with the J_{sc} value obtained from experimental *J*–*V* measurement. Moreover, the PSC based on PTAA:PFB-TFSI exhibits higher IPCE than the PSC based on PTAA:Li-TFSI/*t*-BP across the entire visible light spectrum.

In addition to improving photovoltaic performance, PFB-TFSI also significantly enhances the long-term stability of PSCs. As shown in Fig. 4a, the unpackaged PSC based on PTAA:PFB-TFSI maintained 90% of its initial PCE after aging for 30 days under ambient air conditions (23 ± 4 °C, 50–70% relative humidity), while the unpackaged PSC based on PTAA:Li-TFSI/*t*-BP only retained 57% of its initial PCE under the same conditions. The long-term stability under high temperature and high humidity conditions is crucial for evaluating the stability of PSCs. Therefore, we conducted damp heat stability tests on unpackaged PSCs continuously heated at 85 °C in ambient air with 50–70% relative humidity. As shown in Fig. 4c, after aging for 300 hours, the PSC based on PTAA:PFB-TFSI maintained

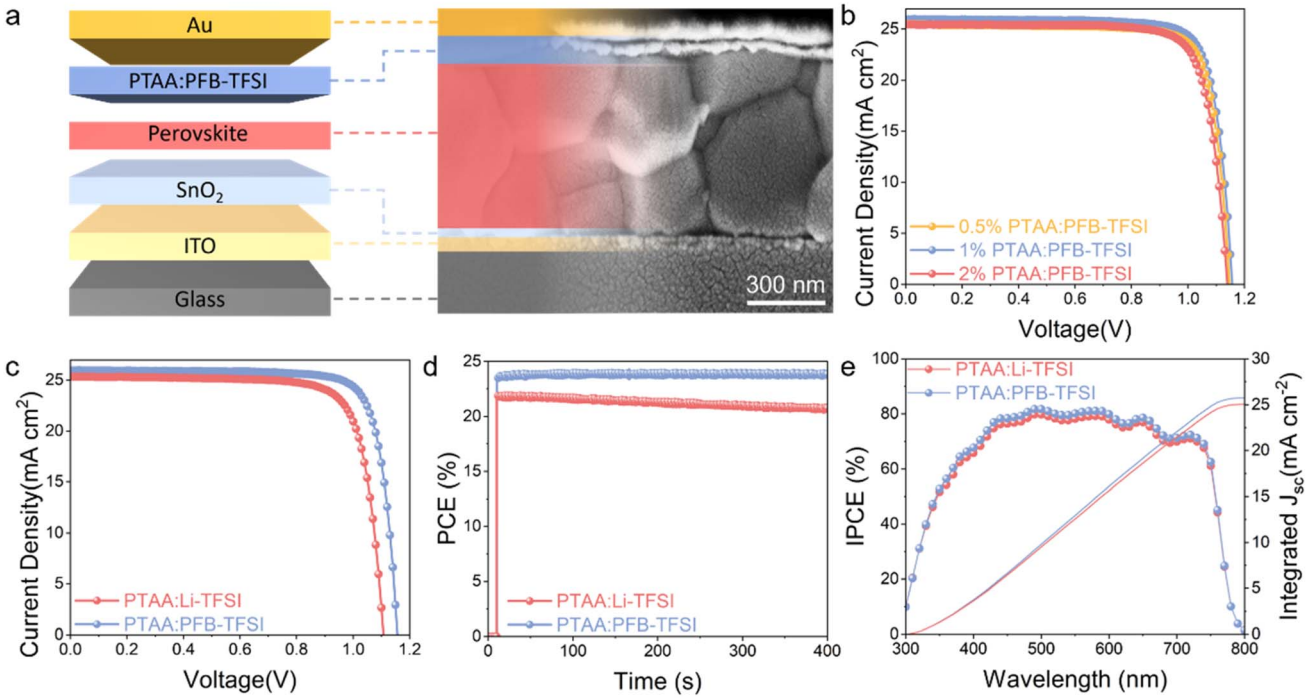

Fig. 3 (a) Cross-section SEM of the PSC based on ITO/SnO_2/perovskite/PTAA:PFB-TFSI/Au. (b) *J*–*V* curves of champion efficiency of PSCs based on PTAA doped with various concentrations of PFB-TFSI. (c) *J*–*V* curves of champion efficiency of PSCs based on PTAA:Li-TFSI/*t*-BP and PTAA:PFB-TFSI. (d) Steady-state PCE outputs at the MPP for PSCs based on PTAA:Li-TFSI/*t*-BP and PTAA:PFB-TFSI. (e) IPCE spectra and integrated current densities for PSCs based on PTAA:Li-TFSI/*t*-BP and PTAA:PFB-TFSI.

88% of its initial PCE, while the PSC based on PTAA:Li-TFSI/*t*-BP retained only 63% of its initial PCE. The improved long-term stability of the PSC based on PTAA:PFB-TFSI is mainly attributed to (1) PFB-TFSI itself having excellent hydrophobicity, which enhances the hydrophobicity of the HTL and reduces the erosion of perovskite by water molecules; (2) PFB-TFSI being able to passivate the surface defects of the perovskite, slowing down the aging and degradation of the perovskite.

As depicted in Fig. S6, when Li-TFSI is placed on the surface of the perovskite and exposed to the ambient environment, hygroscopic Li-TFSI absorbs moisture from the air, leading to significant degradation of the perovskite film. Additionally, the polar solvent *t*-BP can also damage the perovskite film. In contrast, PFB-TFSI, being non-hygroscopic, does not affect the underlying perovskite layer even after being exposed to the ambient environment for 30 days.

Further measurements of the water contact angles of Li-TFSI/*t*-BP and PFB-TFSI doped PTAA films were conducted to study the hydrophobic properties (Fig. 4b). The initial water contact angle of the PTAA:Li-TFSI/*t*-BP film was 87.86°; due to Li-TFSI absorbing moisture from the air, the contact angle decreased to 78.26° after 9 minutes. In contrast, owing to the excellent hydrophobicity of PFB-TFSI, the initial water contact angle of PTAA:PFB-TFSI film reached 96.6°. After being exposed to the ambient environment for 9 minutes, the water contact angle remains at 89.98°. This demonstrates that compared to the PTAA:Li-TFSI/*t*-BP film, the PTAA:PFB-TFSI film exhibits superior hydrophobicity and stability, effectively preventing moisture from infiltrating the perovskite layer.[44]

Moreover, to visually assess the impact of PTAA film morphology on the performance and stability of PSCs, AFM and SEM images were obtained for PTAA:Li-TFSI/*t*-BP and PTAA:PFB-TFSI films. First, SEM images of freshly prepared PTAA:Li-TFSI/*t*-BP and PTAA:PFB-TFSI films were obtained (Fig. S7). Due to the hygroscopic nature of Li-TFSI, moisture easily infiltrates the underlying layers. SEM images of PTAA:Li-TFSI/*t*-BP and PTAA:PFB-TFSI films after aging for 15 days at 23 ± 4 °C in ambient air with 50–70% relative humidity were obtained and are shown in Fig. 4d. Numerous white fluffy substances and pores were clearly observed on the PTAA:Li-TFSI/*t*-BP film. The former are byproducts of the oxidation process, denoted as Li_xO_y, while the latter are pores left by the volatilization of *t*-BP, providing pathways for moisture intrusion into the perovskite. These factors contribute to the inferior stability of the HTL doped with Li-TFSI/*t*-BP. In contrast, due to the non-hygroscopic nature of PFB-TFSI, the PTAA:PFB-TFSI film maintains its original morphology well after aging for 15 days under the same conditions. As shown in the AFM images in Fig. 4e and f, the root mean square (RMS) of the PTAA:Li-TFSI/*t*-BP film reaches 7.07 nm, while the surface RMS of the PTAA:PFB-TFSI film is only 5.88 nm. Additionally, Kelvin Probe Force Microscopy (KPFM) was performed to characterize the surface potentials of PTAA:Li-TFSI/*t*-BP and PTAA:PFB-TFSI films (Fig. S8). The distribution of surface potential and average value are shown. The average surface potential of the PTAA:PFB-TFSI film (25 mV) is lower than that of PTAA:Li-TFSI/*t*-BP (30 mV). The corresponding RMS values of PTAA:Li-TFSI/*t*-BP and PTAA:PFB-TFSI films are 6.5 and 5.2 mV, respectively.

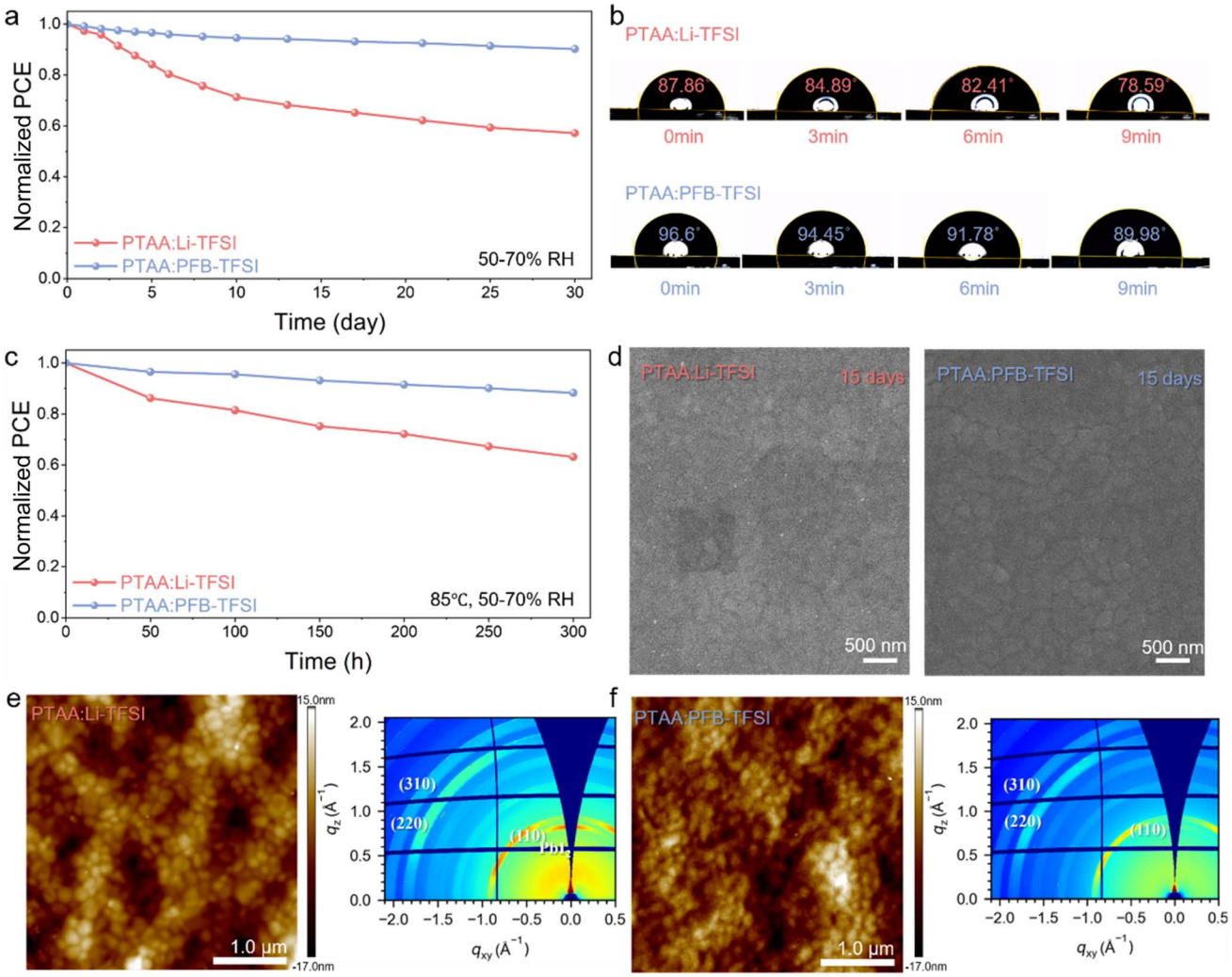

Fig. 4 (a) Moisture stability of unencapsulated PSCs based on PTAA:Li-TFSI/*t*-BP and PTAA:PFB-TFSI. (b) Water contact angles of PTAA:Li-TFSI/*t*-BP and PTAA:PFB-TFSI films. (c) Damp thermal stability of unencapsulated PSCs based on PTAA:Li-TFSI/*t*-BP and PTAA:PFB-TFSI. (d) SEM images of the aged PTAA:Li-TFSI/*t*-BP and PTAA:PFB-TFSI films. AFM topographical images and 2D-GIXD images of (e) aged PTAA:Li-TFSI/*t*-BP film and (f) aged PTAA:PFB-TFSI film on the perovskite layer.

The reduced RMS of the PTAA:PFB-TFSI film indicates that the uniformity of surface potential is enhanced, which is beneficial for improving the charge transfer efficiency and enhancing the device efficiency.

In addition, the stabilities of perovskite covered with PTAA:Li-TFSI/*t*-BP and PTAA:PFB-TFSI films were tested using XRD.[45,46] As shown in Fig. S9, samples show the typical diffraction peaks of perovskite films. Due to the hygroscopic nature of Li-TFSI and the presence of pores in the film, the Li-TFSI-doped samples exhibit distinct PbI_2 characteristic peaks after 15 days of aging, indicating perovskite degradation. In contrast, after aging for 15 days, no obvious PbI_2 characteristic peak is observed in the PFB-TFSI-doped samples. To further investigate the degradation process of perovskite films, 2D Grazing Incidence X-ray Diffraction (2D-GIXD) of the relevant samples with the ITO/SnO_2/perovskite/HTL structure was performed. As shown in Fig. 4e and f, after aging for 30 days at 23 ± 4 °C with 50–70% relative humidity in air, the samples doped with PFB-TFSI and Li-TFSI/*t*-BP exhibit diffraction rings with different intensities at $q \approx 10$, 20, and 23.5 nm^{-1}, corresponding to the (110), (220), and (310) crystal planes of perovskite, respectively. Compared to the PTAA:PFB-TFSI samples, the PTAA:Li-TFSI/*t*-BP samples show a clearer and more distinct diffraction ring at $q \approx 9$ nm^{-1}, which is related to the degradation of perovskite and the formation of PbI_2. These results demonstrate that due to the non-ionic structure and hydrophobicity of PFB-TFSI, as well as its solubility in chlorobenzene, the PTAA:PFB-TFSI film has a smoother and more uniform surface morphology compared to the PTAA:Li-TFSI/*t*-BP film. It effectively blocks the intrusion of water molecules to protect the perovskite layer, thereby ensuring good long-term stability of PSCs based on PTAA:PFB-TFSI.

3. Conclusion

In summary, a novel fluorinated molecule PFB-TFSI is developed as a p-dopant for PTAA in PSCs. PFB-TFSI has good solubility and hydrophobicity, and its lower HOMO level can directly

oxidize PTAA to generate $[PTAA]^+$ radical cations without post-treatment. In addition, F and O atoms in PFB-TFSI can passivate perovskite defects. Compared to 21.98% PCE of the PSC based on PTAA:Li-TFSI/*t*-BP, the PSC based on PTAA:PFB-TFSI achieved a higher PCE of 24.22%. Moreover, the long-term stability of the PSC based on PTAA:PFB-TFSI is greatly improved, retaining 90% of its initial PCE after aging for 30 days at 23 ± 4 °C and 50–70% relative humidity, whereas the PSC based on PTAA:Li-TFSI/*t*-BP only retains 57%. Furthermore, after aging for 300 hours at 85 °C in ambient air with 50–70% relative humidity, the PSC based on PTAA:PFB-TFSI maintained 88% of its initial PCE, while the PSC based on PTAA:Li-TFSI/*t*-BP retained only 63%. This work successfully developed a non-ionic p-dopant based on the Li-TFSI structure, achieving effective doping of PTAA and ultimately improving the efficiency and long-term stability of PSCs.

Author contributions

Z. Wan conceived the eida for the project. W. Yu and J. Yang fabricated and characterized the divices. Y. Zhang and Y. Wang performed and discussed the DFT calculations. R. Wei participated in the characterization of other properties. Z. Wan, W. Yu, J. Yang and Y. Zhang analyzed all data and wrote the manuscript. M. Azam contributed to refining the language. Z. Wan and W. Yu contributed to revising the manuscript. Z. Wan, J. Luo and C. Jia supervised the project.

Conflicts of interest

The authors declare no conflict of interest.

Data availability

Further details of the experimental procedure, CV, differential charge map, destructive test, SEM, KPFM, and XRD data are available in the SI. See DOI: https://doi.org/10.1039/d5sc04440e.

Acknowledgements

The authors are grateful to the National Natural Science Foundation of China (No. 62374029, 22175029, 62474033 and W2433038), the Young Elite Scientists Sponsorship Program by CAST (No. YESS20220550), the Sichuan Science and Technology Program (No. 2024NSFSC0250), the Natural Science Foundation of Shenzhen Innovation Committee (JCYJ20210324135614040) and the Fundamental Research Funds for the Central Universities of China (No. ZYGX2022J032).

References

1 A. Kojima, K. Teshima, Y. Shirai, *et al.*, Organometal Halide Perovskites as Visible-Light Sensitizers for Photovoltaic Cells, *J. Am. Chem. Soc.*, 2009, **131**, 6050–6051.
2 H. Oga, A. Saeki, Y. Ogomi, *et al.*, Improved Understanding of the Electronic and Energetic Landscapes of Perovskite Solar Cells: High Local Charge Carrier Mobility, Reduced Recombination, and Extremely Shallow Traps, *J. Am. Chem. Soc.*, 2014, **136**, 13818–13825.
3 J. Lim, M. T. Hörantner, N. Sakai, *et al.*, Elucidating the long-range charge carrier mobility in metal halide perovskite thin films, *Energy Environ. Sci.*, 2019, **12**, 169–176.
4 S. D. Stranks, G. E. Eperon, G. Grancini, *et al.*, Electron-Hole Diffusion Lengths Exceeding 1 Micrometer in an Organometal Trihalide Perovskite Absorber, *Science*, 2013, **342**, 341–344.
5 J. Park, J. Kim, H.-S. Yun, *et al.*, Controlled growth of perovskite layers with volatile alkylammonium chlorides, *Nature*, 2023, **616**, 724–730.
6 National Renewable Energy Laboratory, *Best Research-Cell Efficiency Chart*, https://www.nrel.gov/pv/cell-efficiency.html.
7 J. X. Xia, J. S. Luo, H. Yang, *et al.*, Vertical Phase Separated Cesium Fluoride Doping Organic Electron Transport Layer: A Facile and Efficient "Bridge" Linked Heterojunction for Perovskite Solar Cells, *Adv. Funct. Mater.*, 2020, **30**, 2001418.
8 Y. B. Wang, Y. F. Yue, X. D. Yang, *et al.*, Toward Long-Term Stable and Highly Efficient Perovskite Solar Cells via Effective Charge Transporting Materials, *Adv. Energy Mater.*, 2018, **8**, 1800249.
9 Z. Xing, S. H. Li, S. H. Yang, *et al.*, Targeted Molecular Design of Functionalized Fullerenes for High-Performance and Stable Perovskite Solar Cells, *Small Struct.*, 2022, **3**, 2200012.
10 J. Burschka, N. Pellet, S. J. Moon, *et al.*, Sequential deposition as a route to high-performance perovskite-sensitized solar cells, *Nature*, 2013, **499**, 316–319.
11 L. Calió, S. Kazim, M. Grätzel, *et al.*, Hole-Transport Materials for Perovskite Solar Cells, *Angew. Chem., Int. Ed.*, 2016, **55**, 14522–14545.
12 M. Kim, J. Jeong, H. Lu, *et al.*, Conformal quantum dot-SnO_2 layers as electron transporters for efficient perovskite solar cells, *Science*, 2022, **375**, 302–306.
13 J. Jeong, M. Kim, J. Seo, *et al.*, Pseudo-halide anion engineering for α-$FAPbI_3$ perovskite solar cells, *Nature*, 2021, **592**, 381–385.
14 H. Min, M. Kim, S.-U. Lee, *et al.*, Efficient, stable solar cells by using inherent bandgap of α-phase formamidinium lead iodide, *Science*, 2019, **366**, 749–753.
15 J. J. Yoo, G. Seo, M. R. Chua, *et al.*, Efficient perovskite solar cells via improved carrier management, *Nature*, 2021, **590**, 587–593.
16 Z. Li, C. Xiao, Y. Yang, *et al.*, Extrinsic ion migration in perovskite solar cells, *Energy Environ. Sci.*, 2017, **10**, 1234–1242.
17 S. Wang, Z. Huang, X. Wang, *et al.*, Unveiling the Role of tBP-LiTFSI Complexes in Perovskite Solar Cells, *J. Am. Chem. Soc.*, 2018, **140**, 16720–16730.
18 W. Li, H. Dong, L. Wang, *et al.*, Montmorillonite as bifunctional buffer layer material for hybrid perovskite solar cells with protection from corrosion and retarding recombination, *J. Mater. Chem. A*, 2014, **2**, 13587–13592.
19 S. Wang, M. Sina, P. Parikh, *et al.*, Role of 4-tert-Butylpyridine as a Hole Transport Layer Morphological Controller in Perovskite Solar Cells, *Nano Lett.*, 2016, **16**, 5594–5600.

20 J. Zhang, T. Zhang, L. Jiang, *et al.*, 4-tert-Butylpyridine Free Hole Transport Materials for Efficient Perovskite Solar Cells: A New Strategy to Enhance the Environmental and Thermal Stability, *ACS Energy Lett.*, 2018, **3**, 1677–1682.

21 N. A. N. Ouedraogo, G. O. Odunmbaku, B. Guo, *et al.*, Oxidation of Spiro-OMeTAD in High-Efficiency Perovskite Solar Cells, *ACS Appl. Mater. Interfaces*, 2022, **14**, 34303–34327.

22 X. Liu, B. Zheng, L. Shi, *et al.*, Perovskite solar cells based on Spiro-OMeTAD stabilized with an alkylthiol additive, *Nat. Photonics*, 2023, **17**, 96–105.

23 J. Kong, Y. Shin, J. A. Röhr, *et al.*, CO_2 doping of organic interlayers for perovskite solar cells, *Nature*, 2021, **594**, 51–56.

24 J. Luo, J. Xia, H. Yang, *et al.*, Toward high-efficiency, hysteresis-less, stable perovskite solar cells: unusual doping of a hole-transporting material using a fluorine-containing hydrophobic Lewis acid, *Energy Environ. Sci.*, 2018, **8**, 2035–2045.

25 N. Sakai, R. Warren, F. Zhang, *et al.*, Adduct-based p-doping of organic semiconductors, *Nat. Mater.*, 2021, **20**, 1248–1254.

26 Y. Liu, Y. Hu, X. Zhang, *et al.*, Inhibited aggregation of lithium salt in spiro-OMeTAD toward highly efficient perovskite solar cells, *Nano Energy*, 2020, **70**, 104483.

27 X. Guo, J. Li, B. Wang, *et al.*, Improving and Stabilizing Perovskite Solar Cells with Incorporation of Graphene in the Spiro-OMeTAD Layer: Suppressed Li Ions Migration and Improved Charge Extraction, *ACS Appl. Energy Mater.*, 2020, **3**, 970–976.

28 L.-L. Jiang, Z.-K. Wang, M. Li, *et al.*, Flower-like MoS_2 nanocrystals: a powerful sorbent of Li^+ in the Spiro-OMeTAD layer for highly efficient and stable perovskite solar cells, *J. Mater. Chem. A*, 2019, **8**, 3655–3663.

29 H. Zhang, Y. Shi, F. Yan, *et al.*, A dual functional additive for the HTM layer in perovskite solar cells, *Chem. Commun.*, 2014, **39**, 5020–5022.

30 K. Wang, X. Liu, R. Huang, *et al.*, Nonionic $Sc_3N@C_{80}$ Dopant for Efficient and Stable Halide Perovskite Photovoltaics, *ACS Energy Lett.*, 2019, **20**, 1852–1861.

31 J.-Y. Seo, H.-S. Kim, S. Akin, *et al.*, Novel p-dopant toward highly efficient and stable perovskite solar cells, *Energy Environ. Sci.*, 2018, **10**, 2985–2992.

32 C. Ming, A. Kerttu, C. Cheng, *et al.*, Acceptor-Donor-Acceptor Type Ionic Molecule Materials for Efficient Perovskite Solar Cells and Organic Solar Cells, *Nano Energy*, 2016, **30**, 387–397.

33 D. Vaitukaityte, C. Momblona, K. Rakstys, *et al.*, Cut from the Same Cloth: Enamine-Derived Spirobifluorenes as Hole Transporters for Perovskite Solar Cells, *Chem. Mater.*, 2021, **33**, 6059–6067.

34 F. Ali, C. Roldán-Carmona, M. Sohail, *et al.*, Applications of Self-Assembled Monolayers for Perovskite Solar Cells Interface Engineering to Address Efficiency and Stability, *Adv. Energy Mater.*, 2020, **13**, 2002989.

35 B. de Boer, A. Hadipour, M. M. Mandoc, *et al.*, Tuning of Metal Work Functions with Self-Assembled Monolayers, *Adv. Mater.*, 2005, **17**, 621–625.

36 F. Ansari, E. Shirzadi, M. Salavati-Niasari, *et al.*, Passivation mechanism exploiting surface dipoles affords high-performance perovskite solar cells, *J. Am. Chem. Soc.*, 2020, **26**, 11428–11433.

37 H. Zhang, F. T. Eickemeyer, Z. Zhou, *et al.*, Multimodal host–guest complexation for efficient and stable perovskite photovoltaics, *Nat. Commun.*, 2021, **12**, 3383.

38 D. Wei, F. Ma, R. Wang, *et al.*, Ion-Migration Inhibition by the Cation-π Interaction in Perovskite Materials for Efficient and Stable Perovskite Solar Cells, *Adv. Mater.*, 2018, **30**, 1707583.

39 R. C. Shallcross, S. Olthof, K. Meerholz, *et al.*, Impact of Titanium Dioxide Surface Defects on the Interfacial Composition and Energetics of Evaporated Perovskite Active Layers, *ACS Appl. Mater. Interfaces*, 2019, **11**, 32500–32508.

40 Y.-S. Jeon, D.-H. Kang, J.-H. Kim, *et al.*, Stability and efficiency improvement of perovskite solar cells by surface hydroxyl defect passivation of SnO_2 layer with 4-fluorothiophenol, *J. Mater. Chem. A*, 2023, **7**, 3673–3681.

41 X. Feng, B. Liu, Y. Peng, *et al.*, Restricting the Formation of Pb-Pb Dimer via Surface Pb Site Passivation for Enhancing the Light Stability of Perovskite, *Small*, 2022, **18**, 2201831.

42 C. Liu, L. Zhang, Y. Li, *et al.*, Highly Stable and Efficient Perovskite Solar Cells with 22.0% Efficiency Based on Inorganic-Organic Dopant-Free Double Hole Transporting Layers, *Adv. Funct. Mater.*, 2020, **30**, 1908462.

43 Y. R. Kim, C. M. Oh, C. J. Yoon, *et al.*, Highly stable and efficient cathode-buffer-layer-free inverted perovskite solar cells, *Nanoscale*, 2021, **11**, 5652–5659.

44 J. Zhang, Y. Hua, B. Xu, *et al.*, The Role of 3D Molecular Structural Control in New Hole Transport Materials Outperforming Spiro-OMeTAD in Perovskite Solar Cells, *Adv. Energy Mater.*, 2016, **6**, 1601062.

45 Q. Chen, J. Wu, X. Wang, *et al.*, 3-Chloroperoxybenzoic acid doping spiro-OMeTAD for improving the performance of perovskite solar cells, *Chem. Eng. J.*, 2022, **450**, 138313.

46 M. Li, Z. K. Wang, Y. G. Yang, *et al.*, Copper Salts Doped Spiro-OMeTAD for High-Performance Perovskite Solar Cells, *Adv. Energy Mater.*, 2016, **6**, 1601156.